Journal of Alloys and Compounds 508 (2010) 463–470

Contents lists available at ScienceDirect

Journal of Alloys and Compounds

journal homepage: www.elsevier.com/locate/jallcom

Fabrication, microstructure and electrocatalytic property of novel nanoporous palladium composites

Xiaoguang Wang, Weimin Wang, Zhen Qi, Changchun Zhao, Hong Ji, Zhonghua Zhang*

Key Laboratory for Liquid-Solid Structural Evolution and Processing of Materials (MOE), School of Materials Science and Engineering, Shandong University, Jingshi Road 73, Jinan 250061, PR China

ARTICLE INFO

Article history:
Received 26 December 2009
Received in revised form 20 August 2010
Accepted 24 August 2010
Available online 24 September 2010

Keywords:
Metals and alloys
Nanostructured materials
Corrosion
Catalysis

ABSTRACT

Nanoporous palladium composites with second phase embeddings can be fabricated through chemical dealloying of a rapidly solidified $Al_{70}Pd_{30}$ alloy in alkaline or acidic solutions under free corrosion conditions. The microstructure of the precursor alloy and as-dealloyed nanoporous composites was characterized using X-ray diffraction, scanning electron microscopy and energy dispersive X-ray analysis. The experimental results show that the precursor alloy is composed of Al_3Pd and Al_3Pd_2 intermetallic compounds, and the resultant composites comprise the nanoporous palladium matrix dealloyed from Al_3Pd and the undealloyed Al_3Pd_2 embeddings. Moreover, the length scale of ligaments/channels in the nanoporous matrix can be adjusted from 3–6 nm to 15–25 nm by simply changing the dealloying solution. The electrochemical experiments demonstrate that these nanoporous Pd composites have high electrochemical active surface areas and exhibit remarkable electrocatalytic activities towards methanol and ethanol oxidation in alkaline media. These novel nanoporous Pd composites will find potential applications in fields of direct alcohol fuel cells, catalysis, sensing, actuation, and especially load-related areas.

1. Introduction

Nowadays, a kind of nanoporous metals with high surface-to-volume ratio have been fabricated by dealloying appropriate binary or ternary alloys [1,2]. Dealloying refers to the selective dissolution of one or more components out of an alloy utilizing different chemical activities of constituent elements under appropriate corrosion conditions, and then the residual inert metal atoms diffuse and agglomerate to form a random porous structure. In the past few years, nanoporous gold (np-Au) made by dealloying homogeneous Au/Ag alloys has received tremendous attention because it exhibits a series of intriguing properties in catalysis, sensing, and surface plasmon resonance, and so on [3–9]. Apart from np-Au, many other kinds of nanoporous metals or alloys have also been extensively investigated including the underlying formation mechanism and their potential applications [10–14]. For example, Hakamada and Mabuchi [13] fabricated nanoporous Ni and Ni–Cu by dealloying as-rolled Ni–Mn and Ni–Cu–Mn alloys. Xu et al. [14] prepared nanoporous Au/Pt from Au–Pt–Cu alloys and investigated their electrocatalytic properties. Recently, some influential reviews on the nanoporous metal formation by dealloying and on the properties of such materials can be found in the August 2009 issue of MRS Bulletin, in which some appealing theoretical and experimental issues are systematically remarked, and simultaneously, the promising prospects of nanoporous materials are further affirmed in the aspects of both fundamental research and practical applications [15,16].

Nanoporous Pd (npPd) is a promising material for catalytic application, hydrogen sensing and hydrogen storage [17–21]. As reported, the formation of npPd is mostly focused on the dealloying of Pd-containing metallic glass (Pd–Ni–P) and single phase solid solution (Pd–Co) [17,19–21]. For these two systems, a suitable electrochemical potential should be applied to facilitate the dissolution of non-noble elements due to their anticorrosive feature in the common electrolytes. In comparison, dealloying phenomenon is prone to occur in Al-based precursor alloys and has been widely used for obtaining Raney catalysts [22–24]. In the past few years, we have successfully fabricated a series of nanoporous metals from corresponding Al–M (M = Au, Ag, Ni, Cu, Pd etc) precursors through a simple chemical dealloying strategy [25–31]. Generally, the formation of nanoporous metals from Al-based alloys normally involves the dealloying of single phase intermetallic compound or two phase systems. Moreover, the microstructure of the resultant nanoporous metals is diverse (homogeneous structure [25,27,29,31], bimodal channel size distributions [26] or composite structure [30]), due to different chemical activities of phases in the precursor alloys and different surface diffusivities of more noble elements along alloy/solution interfaces in the dealloying process.

* Corresponding author. Tel.: +86 531 88396978; fax: +86 531 88395011.
E-mail address: zh_zhang@sdu.edu.cn (Z. Zhang).

0925-8388/$ – see front matter © 2010 Elsevier B.V. All rights reserved.
doi:10.1016/j.jallcom.2010.08.094

In the present work, we aim to investigate the chemical dealloying of the two phase Al–Pd alloy ($Al_{70}Pd_{30}$) in both alkaline and acidic solutions and the formation of npPd composite structures. In addition, we have also probed the electrochemical properties of these resultant npPd composites, and especially have evaluated the electrocatalytic activities of these composites towards methanol and ethanol electro-oxidation in alkaline media to explore their potential applications in direct alcohol fuel cells (DAFCs).

2. Experimental

2.1. Preparation of precursor alloy and as-dealloyed samples

The $Al_{70}Pd_{30}$ (nominal composition, at.%) alloy used in this work was prepared from elemental Al (purity, 99.95 wt.%) and Pd (purity, 99.9 wt.%) in a quartz crucible using a high-frequency induction furnace. Using a single roller melt spinning apparatus, the pre-alloyed ingots were remelted by high-frequency induction heating in a quartz tube and then melt-spun onto a copper roller with a diameter of 0.35 m at a rotation speed of 1000 revolutions per minute (rpm) in a controlled argon atmosphere. The ribbons obtained were typically 20–50 μm in thickness, 2–4 mm in width and several centimeters in length. The rapidly solidified $Al_{70}Pd_{30}$ ribbons were dealloyed in a 20 wt.% NaOH or 5 wt.% HCl aqueous solution under free corrosion conditions firstly at ambient temperature and then at 90 ± 5 °C until no visible bubbles emerged.

2.2. Microstructural characterization

Phase identification of the starting $Al_{70}Pd_{30}$ alloy and as-dealloyed samples was performed using an X-ray diffractometer (Philips X'Pert) with Cu Kα radiation. The microstructure of the starting $Al_{70}Pd_{30}$ alloy was observed using a scanning electron microscope (LEO 1530 VP) in a back scattered electron mode, and that of the as-dealloyed samples was characterized by SEM in an Inlens mode. The chemical compositions of the starting $Al_{70}Pd_{30}$ alloy and as-dealloyed samples were determined using an energy dispersive X-ray (EDX) analyzer which was attached to SEM.

2.3. Electrochemical measurements

Electrochemical measurements were performed in a standard three-electrode cell using a LK 2005A Potentiostat. The work electrodes, coated by the as-dealloyed npPd composite samples, were prepared as follows: 4 mg fine ground npPd composite sample, 4 mg Vulcan XC-72 carbon powders, 300 μL isopropanol, and 100 μL Nafion solution (0.5 wt.%) were ultrasonically mixed. Then, 5 μL of this homogeneously mixed ink was dropped on a freshly polished glassy carbon (GC) electrode with a diameter of 4 mm and dried at room temperature. Each electrode contained ca. 0.398 mg cm^{-2} of npPd composite samples. The counter electrode was a bright Pt plate, and a saturated calomel electrode (SCE) or a Hg/HgO (1.0 M KOH) electrode (MMO) was used as the reference electrode, depending on experimental requirements. The geometric surface area of each electrode was used to normalize the current density. Voltammetric behavior was characterized in a 0.5 M H_2SO_4 solution deaerated with N_2. The CO stripping experiments were performed by firstly maintaining the work electrode in the 0.5 M H_2SO_4 solution saturated with high purity CO gas at the potential of −0.09 V (vs. SCE) for the period of 600 s, and then transferring the electrode into a clean 0.5 M H_2SO_4 solution followed by a CV scan at a scan rate of 50 mV s^{-1}. The electrocatalytic activity measurements were carried out in solutions of 1.0 M KOH + 0.5 M methanol and 1.0 M KOH + 0.5 M ethanol, respectively. All electrochemical experiments were performed at ambient temperature (~25 °C).

3. Results and discussion

3.1. Microstructure of the precursor alloy and the as-dealloyed samples

Fig. 1 shows the XRD patterns of the $Al_{70}Pd_{30}$ alloy and the corresponding as-dealloyed sample prepared in the 20 wt.% NaOH solution. Before dealloying, the $Al_{70}Pd_{30}$ alloy contains two distinct phases: Al_3Pd (unknown structure, PDF No. 44-1021) and Al_3Pd_2 (hP5, P-3m1, PDF No. 53-0564) intermetallic compounds. After dealloying, the Al_3Pd phase was replaced by fcc Pd phase, indicating that the Al_3Pd phase has been fully dealloyed in the 20 wt.% NaOH solution. However, the diffraction lines associated with the Al_3Pd_2 phase are still visible. Obviously, the Al_3Pd_2 phase is inert to the alkali-attack and retained in the as-dealloyed ribbons. When performing dealloying in the 5 wt.% HCl solution, the same phenomenon can be observed.

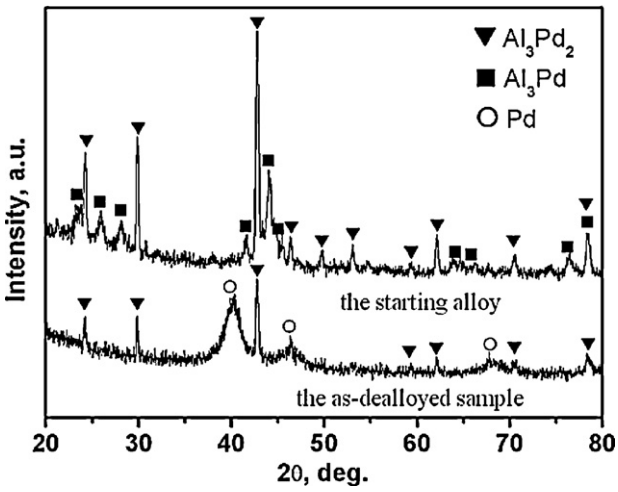

Fig. 1. XRD patterns of the starting $Al_{70}Pd_{30}$ alloy and corresponding as-dealloyed samples in the 20 wt.% NaOH solution.

Fig. 2a shows the section-view microstructure of the $Al_{70}Pd_{30}$ alloy ribbons. It reveals that two distinct phases exist in the alloy, as marked by A and B in Fig. 2a. The EDX analysis demonstrates that the atomic ratio of Al/Pd in A and B is close to 3:2 and 3:1, identical to the stoichiometric ratio of Al_3Pd_2 and Al_3Pd, respectively (Fig. 2b). In combination with the XRD results, it can be further

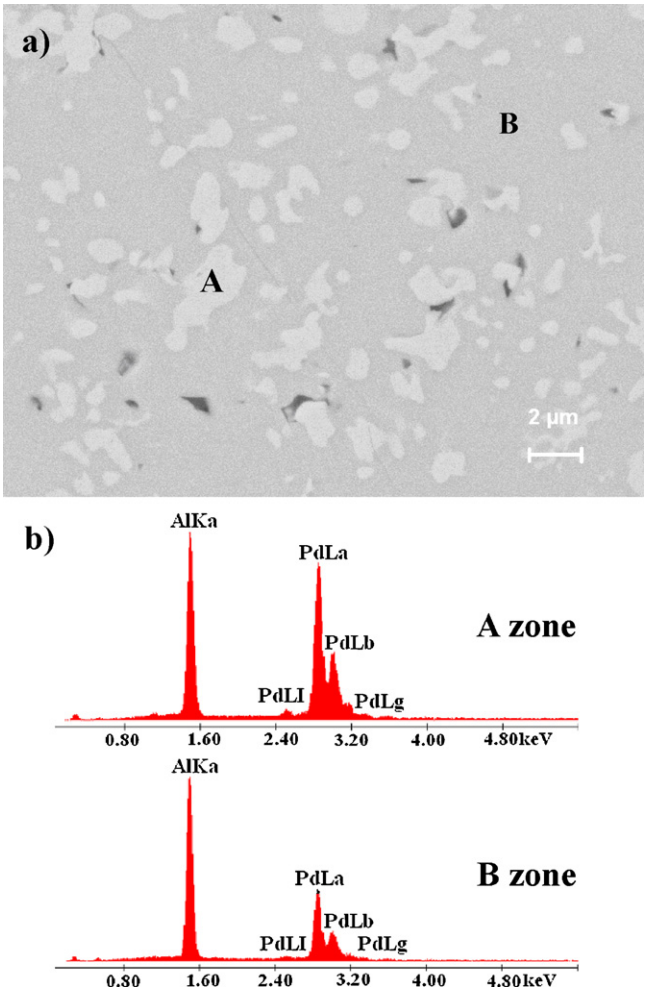

Fig. 2. (a) SEM image showing the section-view microstructure of the $Al_{70}Pd_{30}$ alloy and (b) EDX spectra corresponding to A and B zones in (a).

confirmed that the A phase is Al_3Pd_2 and the B phase is Al_3Pd in the precursor alloy. Moreover, the Al_3Pd phase exhibits a continuous contour throughout the entire ribbon. In contrast, the Al_3Pd_2 phase shows a scattered distribution with sizes ranging from hundreds of nanometers to several microns. There exists a compact adhesive interface between these two distinct phases so that the whole precursor alloy ribbon takes on a monolithic character.

Fig. 3 shows the microstructure of the as-dealloyed samples in the 20 wt.% NaOH solution. It is obvious that the surface of the ribbons comprises two distinct zones: the compact humps and the porous matrix, marked by A and B respectively (Fig. 3a). These humps exhibit dimensions ranging from hundreds of nanometers to several microns. Although a few cracks can be discerned (as marked by downward arrows in Fig. 3a), the monolithic character of the ribbon is well preserved even suffering an alkali-attack dealloying. The EDX results (Fig. 3b) reveal that the composition of humps (A zone) is close to that of Al_3Pd_2 (unchanged after dealloying). In contrast, the continuous matrix (B zone) mainly comprises Pd and only a minor of Al can be detected (several atom percent). It can be further confirmed that the Al_3Pd phase has been fully dealloyed while the Al_3Pd_2 phase is intact. From the high magnification SEM images (Fig. 3c and d), it is clear that the as-dealloyed zones exhibit an open, bicontinuous interpenetrating ligament-channel structure. The length scale of ligaments/channels, by an average of more than 50 ligaments in the nanoporous matrix, is in the range of 3–6 nm. Moreover, the well-combined interfaces can still be observed between the Al_3Pd_2 embeddings and the nanoporous Pd surroundings (highlighted by arrows in Fig. 3c and d). From section-view images (Fig. 3e and f), it can be seen that the distribution of the embeddings (A) and nanoporous matrix (B) is also ubiquitous in the interior of the as-dealloyed ribbons, inheriting the same arrangement of the initial two phases (Al_3Pd_2 and Al_3Pd) in the starting alloy. This resulting composite structure is similar to that of the two phase composite with a nanoporous Pt matrix and [Pt] embeddings reported by Jin et al. [32]. Here, we define these as-prepared two phase npPd composites as npPdCs.

Fig. 4a shows the section-view microstructure of the as-dealloyed samples prepared in the 5 wt.% HCl solution. It is clear that the acid-dealloyed sample also exhibits a two phase composite structure: Al_3Pd_2 embeddings (A) and continuous npPd matrix (B), which can be confirmed by the corresponding EDX results (Fig. 4b). Obviously, Al_3Pd_2 is inert not only in the NaOH solution but also in the HCl solution even at high temperatures ($90 \pm 5\,^{\circ}C$). In contrast, the Al_3Pd phase can be fully dealloyed to form continuous npPd matrix in both corrosive electrolytes. From the SEM images with higher magnifications, it can be seen that the nanoporous/embedding structure is obvious (Fig. 4c and d). Interestingly, the scales of ligaments/channels are modulated to 15–25 nm, obviously larger than those of the alkali-dealloyed npPdCs. Moreover, the interface between the matrix and the embeddings is also discernable (highlighted by arrows in Fig. 4c and d). In our previous research, the ligament coarsening phenomenon is also observed when performing dealloying of other Al-based alloys in HCl solutions [25,26,30]. For example, the length scales of ligaments/channels in np-Au can be modulated from 10–20 to 60–80 nm by just replacing NaOH solutions with HCl solutions [25,26]. It is well established that porosity evolution refers to a complicated self-assembly process involving etching of the less noble metal coupled with coarsening of the more noble one by surface diffusion [33]. It has also been reported that the adsorption of Cl^- ions can increase the surface diffusion rate of Au atoms during the coarsening process of np-Au [34]. Therefore, it is reasonable to assume that Cl^- ions in the HCl solution can accelerate the surface diffusion of Pd atoms and play an important role in the ligament coarsening of the npPd matrix, which is similar to the case of np-Au in the HCl solutions [25,26].

This typical dealloying process related to two phase alloys can be schematically illustrated in Fig. 5. The selective dissolution of the less noble element takes place in the active phase when subjected to the alkali- or acid-attack during the dealloying of a two phase alloy. In contrast, the inert phase is stable against the alkali- or acid-attack and left behind intactly. During the dealloying process, the initial alternating distribution of the two phases in the precursor alloy can be conserved into the as-dealloyed samples. Ultimately, these two distinct dealloying–undealloying processes contribute to the formation of a porosity/embedding composite structure (Fig. 5b). Pugh et al. [35] have argued that if multiple phases exist in an A_xB_{1-x} alloy (here, A is a less noble element and B is a more noble element), typically only the A-rich phase will be dealloyed. In this case, dealloying will be isolated to only surface grains unless a mechanism exists for the penetration of the electrolyte throughout the entire alloy. Lu et al. [36] have also suggested that both the alloy composition and the penetration of the electrolyte throughout the whole precursors play key roles in determining whether dealloying will occur in multiple-phase alloys. In the present work, both Al_3Pd and Al_3Pd_2 existing in the $Al_{70}Pd_{30}$ ribbons belong to intermetallic compounds, and the Al_3Pd phase contains more Al atoms (less noble element) as compared with Al_3Pd_2. According to the arguments of Pugh et al. [35], it is easy to understand that the Al_3Pd phase can be fully dealloyed in the NaOH or HCl solution under free corrosion conditions. Furthermore, the dealloying of the active Al_3Pd phase can provide a percolating path for the penetration of the electrolytes throughout the whole ribbons owing to the continuous feature of Al_3Pd in the $Al_{70}Pd_{30}$ alloy (Figs. 2a and 5). However, the Al_3Pd_2 phase cannot be dealloyed under the same conditions though it is also Al-rich (60 at.% Al). Whether a solid solution or an intermetallic compound can be successfully dealloyed or not, not only is it associated with the atomic percent of the less noble element in the precursors but also with the related intrinsic nature of the constitutive elements and phases. Besides, in the case of two phase alloy systems, the interactions between coexistent phases are widespread and complicated during dealloying. We have systematically investigated the electrochemical dealloying of Al-based (Ag, Au, Cu, and Pd) alloys under potential control, and have found that the critical potentials of some constitutive phases (such as Al_3Pd_2 and Ag_2Al) can even be comparable to the corrosive potentials of corresponding pure noble elements (Pd and Ag, respectively) [37]. In addition, the promoting effect of the less noble phase (Al_3Pd) on the dealloying of the more noble phase (Al_3Pd_2) is imperceptible. The inert Al_3Pd_2 phase is retained in the npPd matrix even under electrochemical conditions. Therefore, it is reasonable to assume that the composition of Al_3Pd_2 goes beyond the parting limit of the Al–Pd system under present corrosion conditions (electroless or potential control). As is known to all, the dealloying of a single phase intermetallic compound generally brings about a uniform porous structure due to the fact that the sharp stoichiometric composition and homogeneous crystal structure ensure the homogeneity at an atomic level [25,38]. In the intermetallic-derived samples, the possible transformation stress and strain during the dealloying process should be the causation of macro- and micro-cracks existing in the resultant nanoporous metals but should have no obvious impact on the formation of the coherent pore distribution. Therefore, the npPd matrix in the npPdCs shows a continuous contour with uniform ligament scales after dealloying in both alkaline and acidic solutions.

3.2. Electrochemical properties of the as-dealloyed nanoporous palladium composites (npPdCs)

For simplicity, the alkali- and acid-dealloyed samples are designated as npPdCs-1 and npPdCs-2, respectively. Fig. 6 shows cyclic voltammetry (CV) curves for the npPdCs-1 and npPdCs-2 electrodes

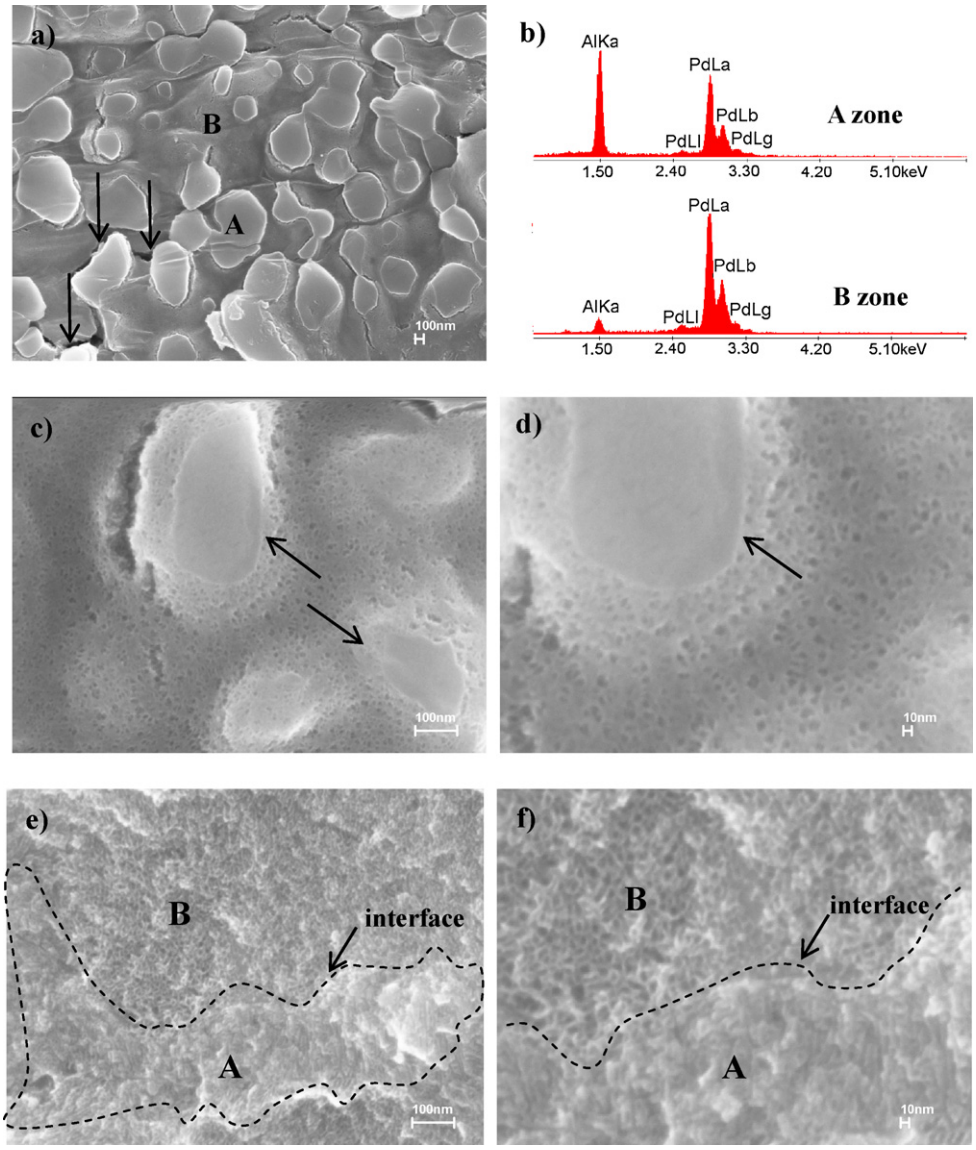

Fig. 3. (a, c and d) Plan-view and (e and f) section-view SEM images showing the microstructure of the npPdCs by dealloying of the $Al_{70}Pd_{30}$ alloy in the 20 wt.% NaOH solution. (b) Corresponding EDX spectra showing the compositions of undealloyed zone (A) and dealloyed zone (B).

in the 0.5 M H_2SO_4 solution at a potential scan rate of 50 mV s^{-1}. From the CVs, there exist two pairs of distinct current peaks in the hydrogen region (A and A′, B and B'), a broad oxidation current peak (C) and a characteristic reduction current peak (C′). The large pair of anodic peaks (A and A′) at a more negative potential is related to H-desorption and -adsorption from the bulk together with the surface of ligaments in the npPd matrix while the small anodic peaks (B and B′) at a more positive potential ascribe to H-desorption and -adsorption on the surface of the npPd ligaments [39,40]. The broad oxidation peak C is ascribed to the formation of Pd surface oxide (PdO) and the corresponding peak C′ is caused by subsequent reduction of the oxide [41,42]. It is well known that an electrochemical process refers to a material/electrolyte interfacial reaction [43]. Thus, the npPd matrix rather than the compact Al_3Pd_2 embeddings should be responsible for the apparent electrochemical features of these typical nanoporous composite structures. Hence, the similar voltammetric behaviors of the npPdCs are obtained compared to those of pure Pd nanostructures [44,45]. Simultaneously, there exist some tiny differences in the CVs of these two npPdCs. The anodic peak A on the CV curve of npPdCs-2 is obviously larger than that of npPdCs-1. This indicates that, in one potential scan, there exists a larger amount of H-absorption for the npPdCs dealloyed in the 5 wt.% HCl solution than those dealloyed in the 20 wt.% NaOH solution, which may be a consequence of different surface crystallographic structures induced by the different corrosive electrolytes.

Fig. 7 shows CV curves for the oxidation of pre-adsorbed CO on the npPdCs-1 and npPdCs-2 electrodes in the 0.5 M H_2SO_4 solution. It is noteworthy that the hydrogen adsorption/desorption peaks of the two electrodes are fully suppressed in the first positive-going scan (solid line) because the pre-adsorbed CO blocks the active surface sites. And then, an anodic peak with a shoulder at the high potential side appears in the potential range from 0.6 to 0.9 V, which is derived from the oxidation of the pre-adsorbed CO. In contrast to the npPdCs-1 electrode, the npPdCs-2 electrode possesses a larger CO stripping peak, indicating that a greater amount of CO molecules adsorb on the active surface of npPdCs-2. Moreover, the simple and sharp line profile of the stripping peak observed for the npPdCs-2 also demonstrates that the surface structure of the samples dealloyed in the HCl solution is relatively homogeneous [46]. After stripping, both the CV curves (dash line) return to the same as those recorded in the blank H_2SO_4 solution (Fig. 6). It indicates that the CO pre-adsorbed on the npPdCs electrodes is thoroughly

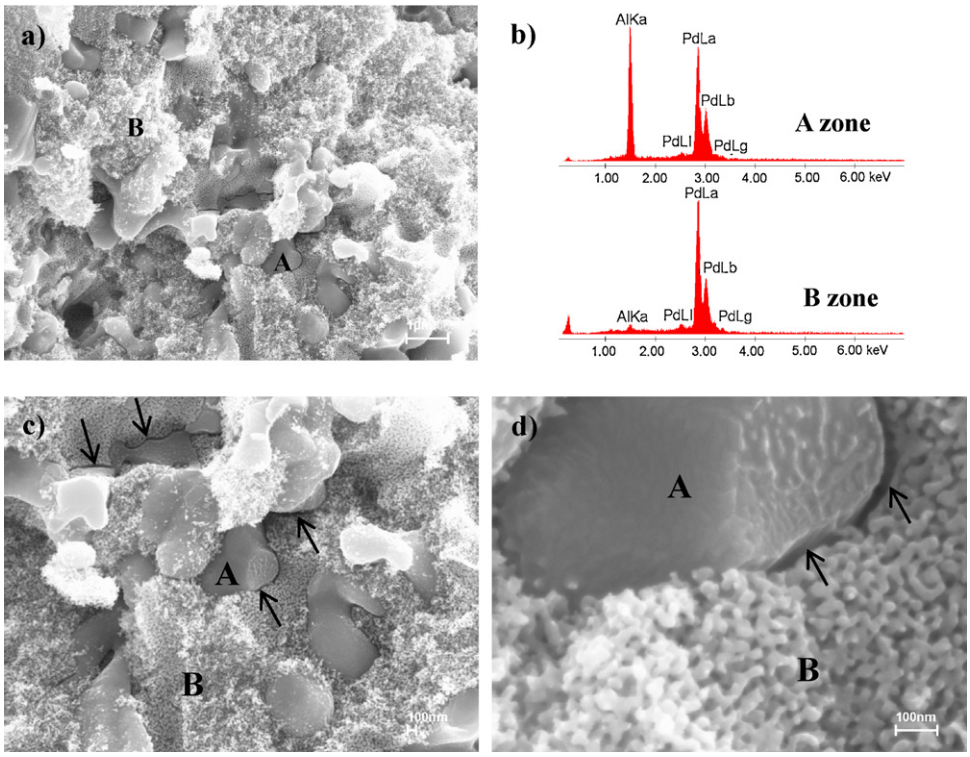

Fig. 4. (a, c and d) Section-view SEM images showing the microstructure of the npPdCs by dealloying of the $Al_{70}Pd_{30}$ alloy in the 5 wt.% HCl solution. (b) Corresponding EDX spectra showing the compositions of undealloyed zone (A) and dealloyed zone (B).

oxidized in the first potential scan and the active sites on the Pd surface recover again. Although CO has been commonly identified as an intermediate and the major poisonous species in the alcohol oxidation process, this unique characteristic, that it is prone to adsorb on the surface active sites of electrocatalysts, has been widely used as an effective method to evaluate the active surface area of electrocatalysts [17,47]. Calculated from the peak area related to CO oxidation in Fig. 7, the consumable charges associated with CO stripping from the npPdCs-1 and npPdCs-2 surfaces are 37.54 and 45.29 mC mg^{-1}, respectively. Assuming the coulombic charge to surface area value of 0.42 mC cm^{-2} for CO stripping on the Pd catalyst surface [44,48], the active surface areas for npPdCs-1 and npPdCs-2 were calculated to be 8.9 and 10.8 $m^2\,g^{-1}$, respectively. Although the length scales of ligaments/channels in the nanoporous matrix of the npPdCs-1 are smaller than those of the npPdCs-2, the active surface area of npPdCs-1 merely attains to about 82.4% of that of npPdCs-2. The smaller active surface area of npPdCs-1 may be attributed to several reasons, such as the liquid sealing effect induced by the microminiature-sized pores, the surface elemental segregation (residual Al) as well as the strong porosity/embedding combination. As reported, the active surface area of pure npPd dealloyed from $Pd_{30}Ni_{50}P_{20}$ metallic glass can attain to 13 $m^2\,g^{-1}$ [17]. It is obvious that such a large number of dispersive compact Al_3Pd_2 embeddings give rise to the decreased active surface area in these npPdCs structures.

Fig. 8 shows the electrocatalytic activities of the npPdCs electrodes towards methanol and ethanol oxidation in alkaline media. Meanwhile, the counterpart, a flat Pd electrode, was also measured for comparison. It is clear that both methanol and ethanol electrooxidation on the three electrodes has been characterized by two

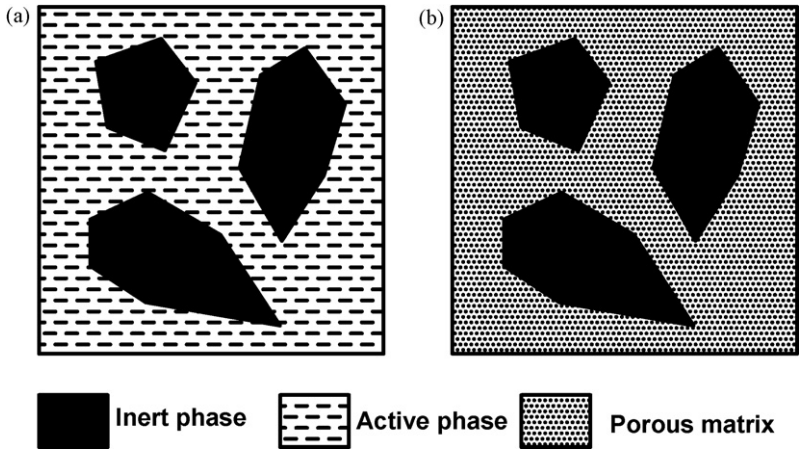

Fig. 5. Schematic illustrations showing the dealloying process of a two phase alloy. (a) The starting two phase alloy and (b) the resulting composites comprising porous matrix and compact embeddings.

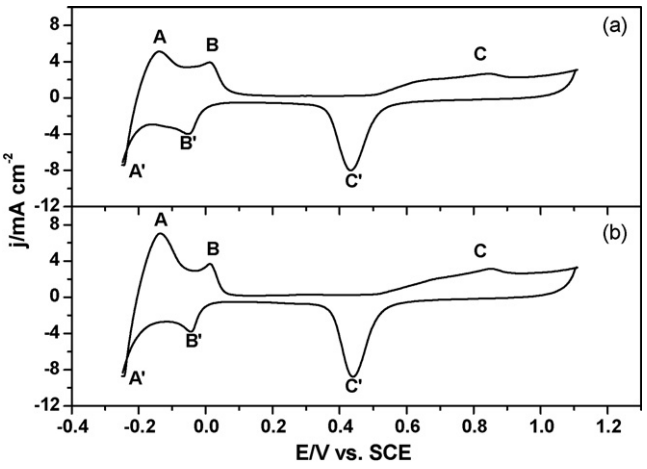

Fig. 6. CV curves of (a) npPdCs-1 and (b) npPdCs-2 electrode in the 0.5 M H_2SO_4 solution deaerated with N_2. The scan rate of potential was 50 mV s^{-1}.

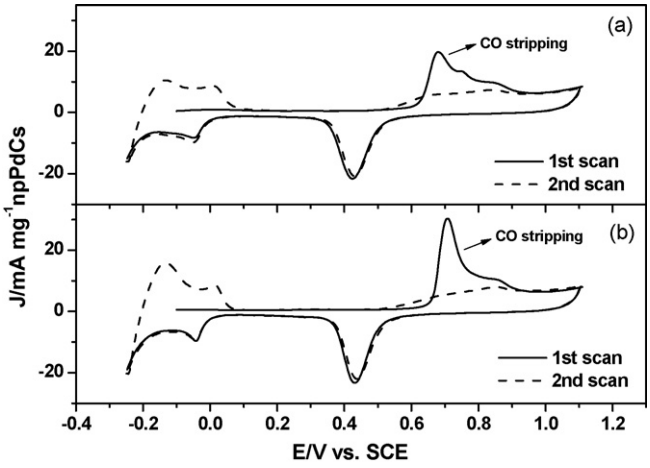

Fig. 7. CO stripping curves obtained on (a) npPdCs-1 and (b) npPdCs-2 electrodes in the 0.5 M H_2SO_4 solution. The scan rate of potential was 50 mV s^{-1}.

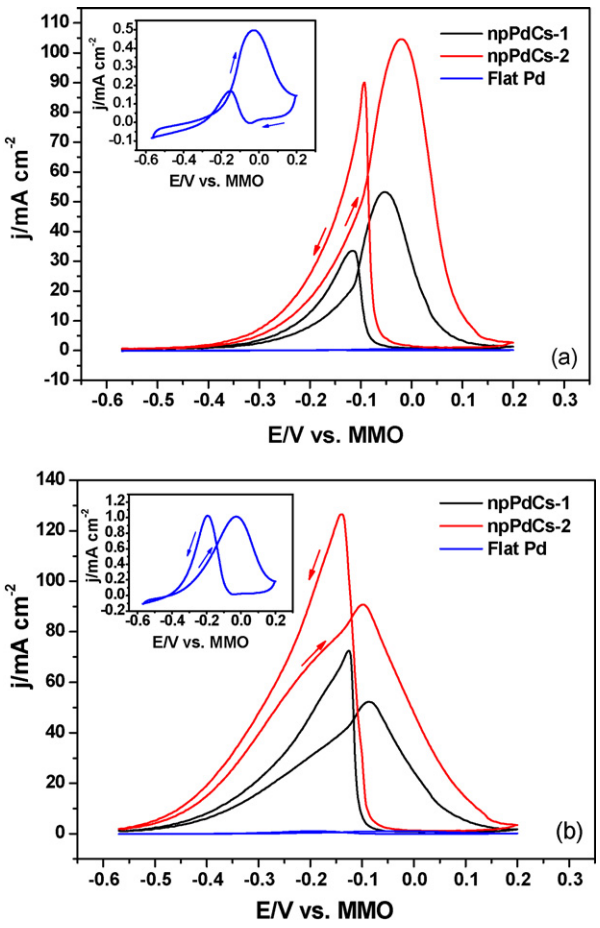

Fig. 8. CV curves recorded in the 1.0 M KOH solution containing (a) 0.5 M methanol and (b) 0.5 M ethanol for the npPdCs-1 electrode (black line), npPdCs-2 electrode (red line), and flat Pd electrode (blue line). The inset in (a) and (b) is the magnified curve from the flat Pd electrode in the corresponding solution. The scan rate of potential was 10 mV s^{-1}. (For interpretation of the references to color in this figure legend, the reader is referred to the web version of this article.)

well-defined anodic peaks. The oxidation peak located in the forward scan is correlated with the oxidation of freshly chemisorbed alcohol molecules, and is normally used to evaluate the catalytic activity of electrocatalysts [49,50]. The CV curves in Fig. 8 were analyzed for the onset potential (E_{op}), oxidation peak current density (j_p), oxidation peak potential (E_p) as well as normalized mass activity (j_m), and their values are shown in Tables 1 and 2 corresponding to the electro-oxidation of methanol and ethanol, respectively.

As seen in Fig. 8a and Table 1, it is clear that both the npPdCs electrodes exhibit much higher catalytic activity for the electro-oxidation of methanol in comparison to the flat Pd counterpart. For example, the E_{op} values of the npPdCs electrodes are more negative as compared to that of the flat Pd electrode, suggesting an improved reaction kinetics of methanol oxidation on the npPdCs. The oxidation peak current density (j_p) attains to 53.41 and 105.16 mA cm^{-2} for the npPdCs-1 and npPdCs-2 electrode, which is 106 and 210 times that obtained on the flat Pd electrode, respectively. Additionally, the mass activity of npPdCs-2 is almost double that of npPdCs-1 despite a little positive shift in the peak potential. The synergistic effect of the enlarged active surface area as well as the increased reaction kinetics may contribute to the higher catalytic activity of npPdCs-2. Similarly, from Fig. 8b and Table 2, it can be seen that both the npPdCs electrodes also exhibit much higher catalytic activity for the electro-oxidation of ethanol as compared to the flat Pd electrode. It should be noted that the onset potentials (E_{op}) as well as the oxidation peak potentials (E_p) of the ethanol electro-oxidation reaction on the npPdCs both shift towards more negative directions in comparison to those of flat Pd, and the values of E_{op} and E_p follow the same order: npPdCs-2 < npPdCs-1 < flat Pd. Moreover, the oxidation peak current density (j_p) of the ethanol

Table 1
Cyclic voltammogram parameters for methanol oxidation on different electrodes in the electrolyte of 1.0 M KOH + 0.5 M CH_3OH.

Electrode	E_{op} (mV)	Forward scan		
		E_p (mV)	j_p (mA cm^{-2})	j_m (mA mg^{-1})
Flat Pd	−228	−25	0.50	–
npPdCs-1	−307	−52	53.41	134.19
npPdCs-2	−366	−21	105.16	264.22

Table 2
Cyclic voltammogram parameters for ethanol oxidation on different electrodes in the electrolyte of 1.0 M KOH + 0.5 M CH_3CH_2OH.

Electrode	E_{op} (mV)	Forward scan		
		E_p (mV)	j_p (mA cm^{-2})	j_m (mA mg^{-1})
Flat Pd	−356	−24	1.03	–
npPdCs-1	−461	−86	52.66	132.31
npPdCs-2	−501	−98	90.64	227.74

electro-oxidation reaches 52.66 and 90.64 mA cm^{-2} for the npPdCs-1 and npPdCs-2 electrode, which is 51 and 88 times that obtained on the flat Pd electrode, respectively. Besides, the mass activity of npPdCs-2 is about 1.72 times that of npPdCs-1.

From the results mentioned above, it can be confirmed that the npPdCs electrodes exhibit higher electrocatalytic activities towards the oxidation of methanol and ethanol as compared with the flat Pd and the npPdCs-2 is superior to the npPdCs-1. The higher catalytic activity of the npPdCs compared to the flat Pd electrode towards the oxidation of small alcohol molecules is mainly ascribed to the reason that the nanoporous ligament-channel matrix offers a large number of active sites (i.e. steps and kinks) for the adsorption and oxidation of these small organic molecules so as to greatly accelerate the reaction kinetics and thus to enhance the reaction efficiency. There is no doubt that the nanoporous structure will greatly increase the active surface area than the flat one. The npPdCs-2 also shows larger active surface area as compared to the npPdCs-1 according to the CO adsorption/stripping measurements (Fig. 7). The enlarged active sites in the npPdCs-2 should be the main reason for its superiority to the npPdCs-1. Of course, the detailed oxidation reaction on the npPdCs catalysts is a complex competitive process involving not only the adsorption and oxidation of alcohol species on the active sites of ligament surfaces but also the continuous mass transport in the interconnected channels. According to the hydromechanics theory, the increase of the fluid resistance leads to the decrease of flux. Obviously, when the size of channels decreases to a certain level, the mass transport in the smaller channels will be largely blocked because of the enlarged fluid resistance. It is helpful to understand the npPdCs-1 with smaller ligaments/channels exhibits less catalytic activity compared to the npPdCs-2. In addition, the more severe liquid sealing and blocking effects should also be responsible for the decreased catalytic activities in the npPdCs-1. Additionally, it is well documented that the electrocatalytic activity will depend on the surface crystallographic structure, the surface electron characteristic as well as the surface segregation of residual elements (residual Al in the present case) [51,52]. For the underlying reason, it still requires a further investigation in future.

Although the Al_3Pd_2 embeddings cannot trigger the electrocatalytic oxidation reaction, it is a promising reinforcement phase considering the compact profile and strong combination with the matrix. And thus, these embeddings can reinforce the matrix against shear localization and critical crack propagation and make nanoporous materials stronger and tougher. In a word, these novel npPdCs can serve as model materials to investigate chemical, physical and mechanical properties of nanoporous metallic materials and will find potential applications in load-related direct alcohol fuel cells, catalysis, sensing, actuation, and so on.

4. Conclusions

In summary, nanoporous Pd composites (npPdCs) can be fabricated through chemical dealloying of the two phase $Al_{70}Pd_{30}$ alloy in alkaline or acidic solutions under free corrosion conditions. The dealloying of the Al_3Pd phase contributes to the formation of npPd matrix while the Al_3Pd_2 phase cannot be dealloyed and retained in the nanoporous matrix as embeddings. The dealloying solutions have a significant influence on the length scales of ligaments/channels in the nanoporous matrix. In addition, the voltammetric behaviors of npPdCs exhibit a similar feature as those of pure Pd nanostructures. As compared with the flat Pd, these novel npPdCs exhibit enhanced electrocatalytic activities towards methanol and ethanol oxidation in alkaline media. Moreover, the npPdCs dealloyed in the HCl solution reveal a superior performance in comparison to those dealloyed in the NaOH solution.

Acknowledgements

The authors gratefully acknowledge financial support by the National Natural Science Foundation of China under grant 50701028 and 50801031, 2nd special support from China Postdoctoral Science Foundation (200902555), and 43rd China Postdoctoral Science Foundation. Z.H. Zhang acknowledges the support from the Alexander von Humboldt Foundation (Germany). The experimental assistance from Ruhr University Bochum (Bochum, Germany) is acknowledged.

References

[1] J. Erlebacher, M.J. Aziz, A. Karma, N. Dimitrov, K. Sieradzki, Nature 410 (2001) 450–453.
[2] J. Snyder, P. Asanithi, A.B. Dalton, J. Erlebacher, Adv. Mater. 20 (2008) 4883–4886.
[3] Y. Ding, J. Erlebacher, J. Am. Chem. Soc. 125 (2003) 7772–7773.
[4] C.X. Xu, J.X. Su, X.H. Xu, P.P. Liu, H.J. Zhao, F. Tian, Y. Ding, J. Am. Chem. Soc. 129 (2007) 42.
[5] Z. Liu, P.C. Searson, J. Phys. Chem. B 110 (2006) 4318–4322.
[6] J. Biener, G.W. Nyce, A.M. Hodge, M.M. Biener, A.V. Hamaza, S.A. Maier, Adv. Mater. 20 (2008) 1211–1217.
[7] J. Biener, A. Wittstock, M.M. Biener, T. Nowitzki, A.V. Hamza, M. Baeumer, Langmuir 26 (2010) 13736–13740.
[8] S.V. Petegem, S. Brandstetter, R. Maass, A.M. Hodge, B.S. El-Dasher, J. Biener, B. Schmitt, C. Borca, H.V. Swygenhoven, Nano Lett. 9 (2009) 1158–1163.
[9] X.Y. Lang, L.Y. Chen, P.F. Guan, T. Fujita, M.W. Chen, Appl. Phys. Lett. 94 (2009) 213109.
[10] H.J. Jin, X.L. Xiao, S. Parida, K. Wang, M. Seo, J. Weissmüller, Nano Lett. 10 (2010) 187–194.
[11] X.Y. Lang, H. Guo, L.Y. Chen, A. Kudo, J.S. Yu, W. Zhang, A. Inoue, M.W. Chen, J. Phys. Chem. C 114 (2010) 2600–2603.
[12] Y.Y. Li, Y. Ding, J. Phys. Chem. C 114 (2010) 3175–3179.
[13] M. Hakamada, M. Mabuchi, J. Alloys Compd. 485 (2009) 583–587.
[14] C.X. Xu, R.Y. Wang, M.W. Chen, Y. Zhang, Y. Ding, Phys. Chem. Chem. Phys. 12 (2010) 239–246.
[15] Y. Ding, M.W. Chen, MRS Bull. 34 (2009) 569–576.
[16] J. Weissmüller, R.C. Newman, H.J. Jin, A.M. Hodge, J.W. Kysar, MRS Bull. 34 (2009) 577–586.
[17] J.S. Yu, Y. Ding, C.X. Xu, A. Inoue, T. Sakurai, M.W. Chen, Chem. Mater. 20 (2008) 4548–4550.
[18] D.Y. Ding, Z. Chen, C. Lu, Sens. Actuator B 120 (2006) 182–186.
[19] M. Hakamada, H. Nakano, T. Furukawa, M. Takahashi, M. Mabuchi, J. Phys. Chem. C 114 (2010) 868–873.
[20] M. Hakamada, M. Mabuchi, J. Alloys Compd. 479 (2009) 326–329.
[21] M. Hakamada, K. Tajima, K. Yoshimura, Y. Chino, M. Mabuchi, J. Alloys Compd. 494 (2010) 309–314.
[22] M. Raney, Ind. Eng. Chem. 32 (1940) 1199–1203.
[23] I. Yamauchi, T. Mase, T. Kajiwara, M. Saraoka, J. Alloys Compd. 348 (2003) 270–277.
[24] I. Yamauchi, H. Kawamura, K. Nakano, T. Tanaka, J. Alloys Compd. 387 (2005) 187–192.
[25] Z.H. Zhang, Y. Wang, Z. Qi, W.H. Zhang, J.Y. Qin, J. Frenzel, J. Phys. Chem. C 113 (2009) 12629–12636.
[26] Z.H. Zhang, Y. Wang, Z. Qi, J.K. Lin, X.F. Bian, J. Phys. Chem. C 113 (2009) 1308–1314.
[27] X.G. Wang, Z. Qi, C.C. Zhao, W.M. Wang, Z.H. Wang, J. Phys. Chem. C 113 (2009) 13139–13150.
[28] Z. Qi, Z.H. Zhang, H.L. Jia, Y.J. Qu, G.D. Liu, X.F. Bian, J. Alloys Compd. 472 (2009) 71–78.
[29] Z. Qi, C.C. Zhao, X.G. Wang, J.K. Lin, W. Shao, Z.H. Zhang, X.F. Bian, J. Phys. Chem. C 113 (2009) 6694–6698.
[30] Z.H. Zhang, Y. Wang, Z. Qi, C. Somsen, X.G. Wang, C.C. Zhao, J. Mater. Chem. 19 (2009) 6042–6050.
[31] Z.H. Zhang, Y. Wang, Y.Z. Wang, X.G. Wang, Z. Qi, H. Ji, C.C. Zhao, Scripta Mater. 62 (2010) 137–140.
[32] H.J. Jin, D. Kramer, Y. Ivanisenko, J. Weissmüller, Adv. Eng. Mater. 9 (2007) 849–854.
[33] C.X. Ji, P.C. Searson, J. Phys. Chem. B 107 (2003) 4494–4499.
[34] R.C. Newman, K. Sieradzki, Science 263 (1994) 1708–1709.
[35] D.V. Pugh, A. Dursun, S.G. Corcoran, J. Mater. Res. 18 (2003) 216–221.
[36] H.B. Lu, Y. Li, F.H. Wang, Scripta Mater. 56 (2007) 165–168.
[37] Q. Zhang, Z.H. Zhang, Phys. Chem. Chem. Phys. 12 (2010) 1453–1472.
[38] S. Kameoka, A.P. Tsai, Catal. Lett. 121 (2008) 337–341.
[39] M. Grdeń, A. Piascik, Z. Koczorowski, A. Czerwiński, J. Electroanal. Chem. 532 (2002) 35–42.
[40] M. Baldauf, D.M. Kolb, Electrochim. Acta 38 (1993) 2145–2153.
[41] L.H. Dall'Antonia, G. Tremiliosi-Filho, G. Jerkiewicz, J. Electroanal. Chem. 502 (2001) 72–81.
[42] M. Grdeń, M. Łukaszewski, G. Jerkiewicz, A. Czerwiński, Electrochim. Acta 53 (2008) 7583–7598.

[43] A.J. Bard, L. Faulkner, Electrochemical Methods: Fundamentals and Applications, Wiley, New York, 1980, pp. 1–43.
[44] W. Pan, X.K. Zhang, H.Y. Ma, J.T. Zhang, J. Phys. Chem. C 112 (2008) 2456–2461.
[45] J.T. Zhang, C.C. Qiu, H.Y. Ma, X.Y. Liu, J. Phys. Chem. C 112 (2008) 13970–13975.
[46] M. Hara, U. Linke, Th. Wandlowski, Electrochim. Acta 52 (2007) 5733–5748.
[47] Y.J. Huang, X.C. Zhou, J.H. Liao, C.P. Liu, T.H. Lu, W. Xing, Electrochem. Commun. 10 (2008) 621–624.
[48] X.G. Li, I.M. Hsing, Electrochim. Acta 51 (2006) 3477–3483.
[49] J. Ye, J. Liu, C. Xu, S.P. Jiang, Y. Tong, Electrochem. Commun. 9 (2007) 2760–2763.
[50] M.W. Xu, G.Y. Gao, W.J. Zhou, K.F. Zhang, H.L. Li, J. Power Sources 175 (2008) 217–220.
[51] N. Tian, Z.Y. Zhou, S.G. Sun, Y. Ding, Z.L. Wang, Science 316 (2007) 732–735.
[52] A. Wittstock, B. Neumann, A. Schaefer, K. Dumbuya, J. Biener, M. Baumer, J. Phys. Chem. C 113 (2009) 5593–5600.